

One Step Diffusion-based Super-Resolution with Time-Aware Distillation

Xiao He¹, Huaao Tang², Zhijun Tu², Junchao Zhang², Kun Cheng¹, Hanting Chen², Yong Guo³, Mingrui Zhu¹, Nannan Wang^{1†}, Xinbo Gao⁴, Jie Hu²

¹ State Key Laboratory of Integrated Services Networks, School of Telecommunications Engineering, Xidian University.

² Huawei Noah's Ark Lab.

³ Consumer Business Group, Huawei.

⁴ Chongqing Key Laboratory of Image Cognition, Chongqing University of Posts and Telecommunications.
nawang@xidian.edu.cn

Abstract—Diffusion-based image super-resolution (SR) methods have shown promise in reconstructing high-resolution images with fine details from low-resolution counterparts. However, these approaches typically require tens or even hundreds of iterative samplings, resulting in significant latency. Recently, techniques have been devised to enhance the sampling efficiency of diffusion-based SR models via knowledge distillation. Nonetheless, when aligning the knowledge of student and teacher models, these solutions either solely rely on pixel-level loss constraints or neglect the fact that diffusion models prioritize varying levels of information at different time steps. To accomplish effective and efficient image super-resolution, we propose a time-aware diffusion distillation method, named TAD-SR. Specifically, we introduce a novel score distillation strategy to align the data distribution between the outputs of the student and teacher models after minor noise perturbation. This distillation strategy enables the student network to concentrate more on the high-frequency details. Furthermore, to mitigate performance limitations stemming from distillation, we integrate a latent adversarial loss and devise a time-aware discriminator that leverages diffusion priors to effectively distinguish between real images and generated images. Extensive experiments conducted on synthetic and real-world datasets demonstrate that the proposed method achieves comparable or even superior performance compared to both previous state-of-the-art (SOTA) methods and the teacher model in just one sampling step. Codes are available at <https://github.com/LearningHx/TAD-SR>.

Index Terms—diffusion model, image super-resolution, face restoration, single-step diffusion distillation.

I. INTRODUCTION

Image super-resolution (SR), a cornerstone task in low-level vision, involves reconstructing high-resolution (HR) images with intricate details from low-resolution (LR) counterparts. Owing to the inherent ill-posed nature of this task, as multiple high-resolution reconstructions are plausible for a given low-resolution input, presenting a persistent and perplexing challenge. Recently, the diffusion model [1], [2], a novel generative model, has garnered increasing attention for its capacity to model complex data distributions. It has gradually emerged as a successor to Generative Adversarial Networks (GANs) [3] in various downstream tasks, including image editing [4], [5], image inpainting [6], [7] and image super-resolution [8], [9].

Specifically, existing diffusion-based image super-resolution methods can be broadly categorized into two streams: one

involves feeding low-resolution images along with noise into the diffusion model as input [8], [9], while the other [10], [11] adapts SR tasks by modifying the sampling process on a pre-trained diffusion model. While these methods have demonstrated promising results, generating HR images typically demands tens or even hundreds of iterative samplings, significantly impeding their practical application and further advancement.

To enhance the inference efficiency of diffusion models, various acceleration techniques have been proposed, such as the development of numerical samplers [19], [20] and the applications of knowledge distillation [21], [22]. However, employing numerical solvers to accelerate sampling speed often compromises performance. Moreover, the majority of methods employing knowledge distillation are tailored for text-to-image generation, where ensuring the diversity of generated images is crucial. In contrast, super-resolution tasks necessitate output images with high visual fidelity relative to LR images. Therefore, directly applying these methods to super-resolution tasks presents significant challenges. For the SR task, ResShift [9] has improved the sampling efficiency of diffusion-based SR models by utilizing information from LR images to reformulate the diffusion process, thereby reducing the number of sampling steps to 15. Furthermore, SinSR [18] merges distillation techniques with a cycle consistency approach to refine the ResShift model into a single inference step. Nonetheless, it still yields blurry results in the high-frequency details of the image, despite ensuring the visual fidelity of the generated image through pixel-level loss constraints. Recently, AddSR [23] employs adversarial diffusion distillation (ADD) [22] for SR task to enhance sampling efficiency while ensuring the perceptual quality of generated images. However, it inherits the issue of image oversaturation present in score distillation sampling. Additionally, it relies on a pre-trained DINOv2 discriminator in pixel space, which is both expensive and challenging to optimize.

To address the issues in the aforementioned methods, we introduce a novel time-aware distillation method to accelerate the sampling rate of diffusion-based SR models. It enables the generation of high-resolution images with fine details in a single sampling step. Specifically, considering that diffusion models focus on high-frequency information at small time steps, we have designed a high-frequency enhanced score

[†]Corresponding Author.

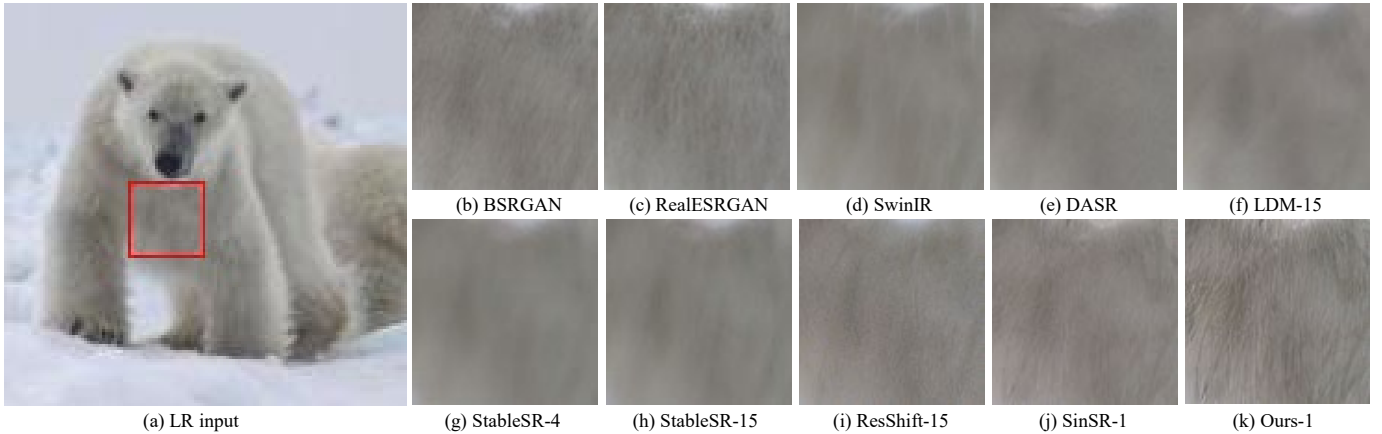


Fig. 1: Qualitative comparisons on one typical real-world example of the proposed method and recent state of the arts, including BSRGAN [12], RealESRGAN [13], SwinIR [14], DASR [15], LDM [16], StableSR [17], ResShift [9], and SinSR [18]. We mark the number of sampling steps of diffusion-based SR method with the format of “Method-A” for more intuitive visualization, where “A” is the number of sampling steps. Note that LDM contains 1000 diffusion steps in training and is accelerated to “A” steps using DDIM [2] during inference. Please zoom in for a better view.

distillation strategy. This strategy refines the student network by evaluating the difference in the distribution of the teacher model and student model outputs after mild noise disturbance, thereby improving the high-frequency details in the generated images of the student model. To overcome the performance limitations of teacher models, we incorporate generative adversarial learning into the distillation framework, forcing the student model to directly generate samples that lie on the manifold of real images in a single inference step. Specifically, we engineer a time-aware discriminator within the latent space that is capable of differentiating between the data distributions of authentic and synthetically generated images subjected to various perturbations. Experimental evidence confirms that the introduction of temporal information into the discriminator significantly enhances its ability to more effectively regulate the generator’s performance.

Overall, our contributions can be summarized as follows:

- We introduce a novel time-aware distillation method that accelerates the diffusion-based SR model into a single inference step.
- To improve the high-frequency details of the generated image, we introduce a novel score distillation method that refines the student model by quantifying the discrepancy in scores between the outputs of the teacher and student models at small time steps.
- Furthermore, to ensure the performance of student model is not solely bound by the teacher model, we incorporate generative adversarial learning into the distillation framework. A key innovation in our approach is the development of a time-aware discriminator. This discriminator is capable of distinguishing between the data distributions of real and generated images that have undergone various perturbations in latent space.
- Extensive experiments on both general and facial datasets have demonstrated that our method, using only single-step sampling, achieves performance that is comparable to or surpasses state-of-the-art methods and teacher models.

II. RELATED WORK

A. Image Super-Resolution.

Traditional methods [24]–[26] for image super-resolution rely on manual design of image priors based on subjective knowledge to restore image details. With the advancement of deep learning (DL), DL-based image super-resolution has become predominant, which mainly focused on network architecture [27]–[30], image priors [31], [32], loss functions [33], [34], and other aspects [13], [35]. Recently, diffusion-based methods for image super-resolution have garnered widespread attention. SR3 [8] incorporated low-resolution images as conditions into the denoising model to guide the sampling process. Subsequently, CDPMSR [36] and IDM [37] respectively utilized preprocessed images and features as conditions to enhance the perceptual quality. In order to reduce the computational cost of the model, StableSR [17] and PASD [38] utilized the powerful generation priors of stable diffusion (SD) [16] to achieve image super-resolution in latent space through diffusion processes. However, these methods typically require dozens or even hundreds of iterations to generate high-resolution images. To enhance the inference efficiency, ResShift [9] redesigned the diffusion process by shifting the residuals between high-resolution and low-resolution images to construct a Markov chain, achieving performance comparable to previous state-of-the-art methods with just 15 sampling steps.

B. Accelerating Diffusion Models.

Although diffusion model [1], [16] has formidable generation capabilities, the substantial number of inference steps poses a significant obstacle to its practical implementation leading to methods reducing the inference steps. Mainstream approaches include the development of high-order samplers [2], [19], [20] and the application of knowledge distillation techniques [21], [22], [39]–[41]. Denoising diffusion implicit

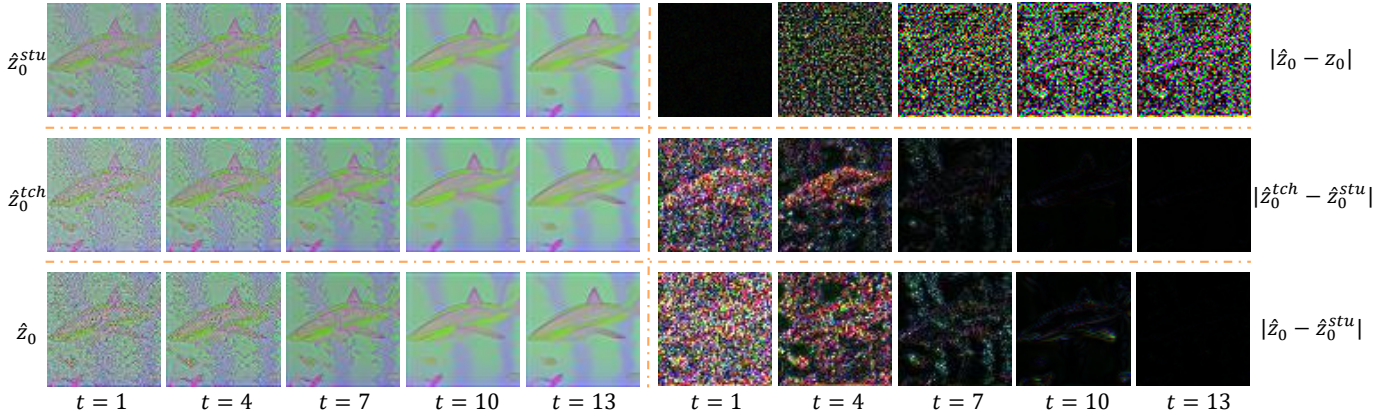


Fig. 2: We inject varying degrees of noise into the outputs of the student model, the teacher model, and the corresponding real data (HR images). These noisy data are then fed into a pre-trained diffusion-based SR model to obtain their denoising scores(visualized as clean data prediction \hat{z}_0).

models (DDIM) [2], an early contribution, introduced a deterministic sampling method that notably decreased the number of diffusion sampling steps. DPMSolver [19] proposed a fast dedicated high-order ODE solver, further reducing the diffusion sampling steps to 20. However, trajectory compression through numerical solvers often results in performance degradation, necessitating over ten inference steps to generate samples. In contrast, progressive distillation [21] gradually reduces the inference steps of student models through multi-stage distillation, but the accumulation of errors in each distillation stage may affect the performance of the student model. Consistency model [40] eliminates the need for computation-intensive iterations by applying consistency regularization to ODE trajectories. Additionally, Adversarial diffusion distillation (ADD) [22] integrates generative adversarial networks with score distillation to enhance the perceptual quality of student network-generated images. For image super-resolution tasks, AddSR [23] introduces two key advancements based on adversarial distillation technology, effectively fulfilling image super-resolution objectives. Inspired by cycle consistency loss, SinSR [18] proposes a single-step image super-resolution method. However, AddSR overlooks the influence of time steps on the discriminator, while SinSR primarily focuses on constraining latent codes through pixel-level loss, neglecting perceptual distribution alignment. To achieve image super-resolution more efficiently and effectively, this work propose a time-aware diffusion distillation method.

III. PRELIMINARY

Diffusion models is a type of probabilistic generative model, which utilize a Markov chain transforms complex data distribution $z_0 \sim p_{data}$ into noise distribution $z_T \sim \mathcal{N}(0, I)$ and recover the data by gradually removing the noise. In image super-resolution tasks, ResShift [9] changes the initial state of diffusion model and constructs a new Markov chains to generate high-resolution images. The forward process can be mathematically expressed as follows:

$$q(z_t|z_0, y) = \mathcal{N}(z_t|z_0 + \eta_t(z_y - z_0), \kappa^2\eta_t I) \quad (1)$$

where z_0 and z_y represent the latent codes obtain by encoding the HR images x and LR images y , respectively. η_t is a serial of hyper-parameters that monotonically increases with timestep t and satisfies $\eta_0 \rightarrow 0$ and $\eta_T \rightarrow 1$, κ is a hyper-parameter controlling the noise variance. Baed on this forward process, the reverse process will commence from the initial state with rich information in low-resolution images to perform denoising. The formula is as follows:

$$q(z_{t-1}|z_t, z_0, y) = \mathcal{N}\left(z_{t-1} \middle| \frac{\eta_{t-1}}{\eta_t} z_t + \frac{\alpha_t}{\eta_t} z_0, \kappa^2 \frac{\eta_{t-1}}{\eta_t} \alpha_t I\right) \quad (2)$$

where $\alpha_t = \eta_t - \eta_{t-1}$, To mitigate the influence of randomness on distillation [18], we reformulate Eq. 2 to employ deterministic sampling, as follows:

$$q(z_{t-1}|z_t, z_0, y) = \delta(k_t z_0 + m_t z_t + j_t z_y) \quad (3)$$

where δ is the unit impulse, $m_t = \sqrt{\frac{\eta_{t-1}}{\eta_t}}$, $j_t = \eta_{t-1} - \sqrt{\eta_{t-1}\eta_t}$ and $k_t = 1 - j_t - m_t$. The details of the derivation can be found in SinSR [18]. In the backward process Eq. 3, x_0 is usually predicted by a trainable deep neural network f_θ with parameter θ . The training objective function of f_θ as follows:

$$\min_{\theta} \sum_t w_t \|f_\theta(z_t, \mathbf{y}, t) - z_0\|_2^2, \quad (4)$$

where $w_t = \frac{\alpha_t}{2\kappa^2\eta_t\eta_{t-1}}$. In practice omitting this weight often leads to performance improvement [1].

Score Distillation Sampling (SDS) is a distillation technique for pre-trained diffusion models, effectively applied in generating 3D assets [42], [43] and accelerating diffusion models [22], [39]. It leverages the rich generative prior of diffusion models to optimize the generated images or the generator, which can be expressed as follows:

$$\nabla_{\theta} \mathcal{L}_{SDS}(z, y, \epsilon, t) = (\epsilon_{\phi}(z_t, y, t) - \epsilon) \frac{\partial z_t}{\partial \theta} \quad (5)$$

where z_t refers to the noised version of z . According to [42], the U-Net jacobian term $\frac{\partial \epsilon_{\phi}(z, y, t)}{\partial z_t}$ is omitted in Eq. 5 to lead an effective gradient.

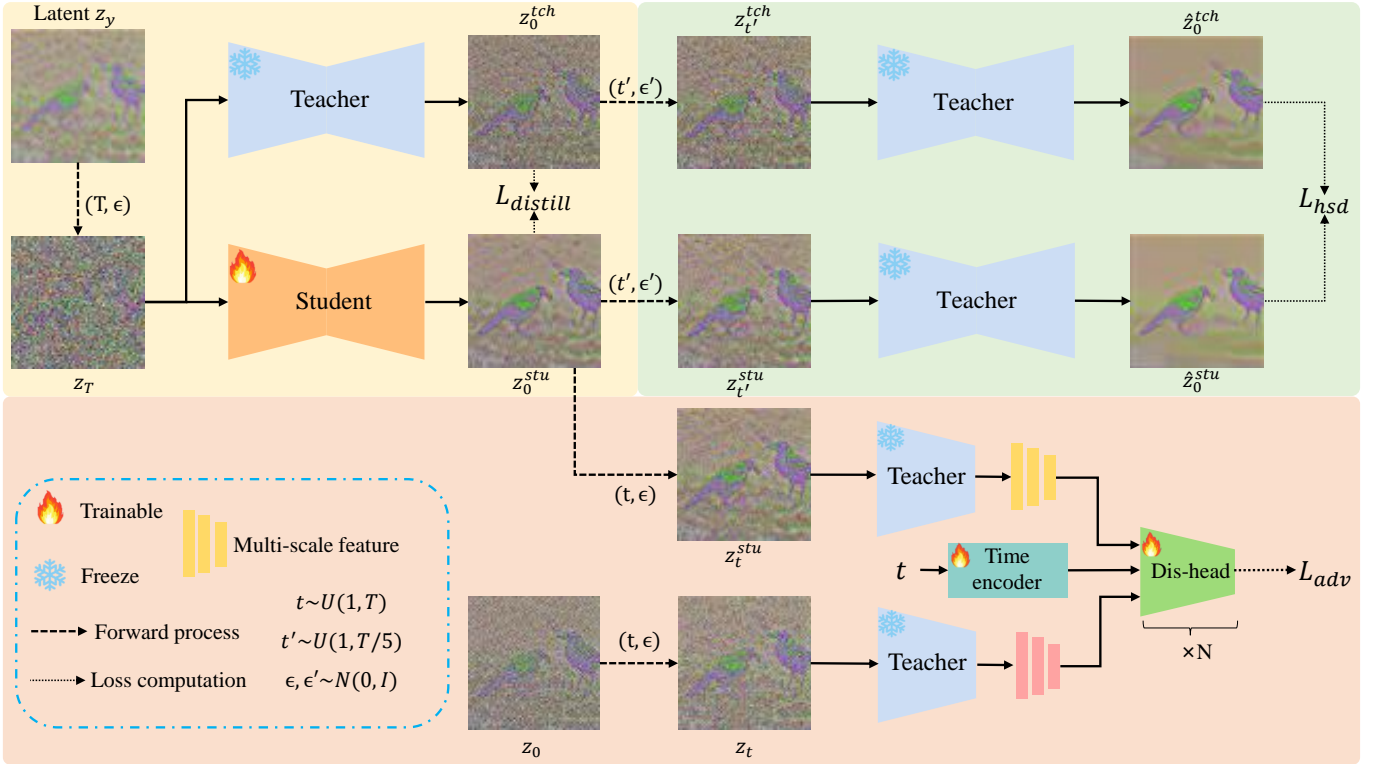


Fig. 3: **Method overview.** We train our student model to map a noisy latent z_T to clean latent z_0^{stu} through single step sampling. To match the student model’s output with the multi-step sampling outputs of the teacher model, we optimize the student model using both vanilla distillation loss and our proposed high-frequency enhanced score distillation. Additionally, to further improve the performance of the student model, we propose a time-aware discriminator that provides effective supervision through generative adversarial training.

IV. METHODOLOGY

A. Motivation

To explore distillation methods more applicable to accelerating diffusion-based SR models, we conducted an experiment to visualize the score differences among the single-step output of the student model, the multi-step output of the teacher model, and the high-resolution images following noise perturbation in latent space. (Note that the student model has the same weight as the teacher model.) Specifically, we re-noise the outputs of the student model, the teacher model, and the real data (HR image) to varying degrees, then feed the noise data into a pre-trained diffusion-based SR model to view the denoising scores (visualized as clean data prediction \hat{z}_0 in Fig. 2) and compare their differences of scores.

From the first row of Fig. 2, it can be seen that even when real data are fed into a well-trained diffusion-based SR model, there is still a gap between the predicted scores \hat{z}_0 and the real scores z_0 . This indicates that even in ideal situations, score-based distillation (SDS) itself has biases, consistent with the conclusions of previous related work [44], [45]. Therefore, utilizing SDS to accelerate diffusion-based SR models is not optimal. To identify the shortcomings of the student model and design a suitable distillation strategy, we further analyzed the score differences $|\hat{z}_0^{tch} - \hat{z}_0^{stu}|$ between the outputs of the teacher and student models after noise disturbance, as

illustrated in the second row of Fig. 2. From the figure, it is evident that there is a notable difference in denoising scores between the output of the teacher model and that of the student model when subjected to minor noise disturbances. Additionally, diffusion models primarily focus on high-frequency information in images at small time steps. Based on these observations, it can be concluded that the student model’s output mainly lacks high-frequency details compared to the teacher model. Therefore, we believe that computing the score differences between the outputs of the teacher and student models under mild noise disturbances can provide an effective gradient direction to guide the optimization of the student model.

In addition, the third row in Fig. 2 visualizes the score difference $|\hat{z}_0 - \hat{z}_0^{stu}|$ between the output of the student model and the real data after noise disturbance. It can be seen that this score difference is significant, and this difference changes with time steps. However, existing methods do not consider this factor when distinguishing the distribution of real data and generated data after noise disturbance. Instead, they directly use a discriminator to distinguish the differences between the data distributions of real and generated images subjected to various perturbations, which poses a challenge to the optimization of the discriminator.

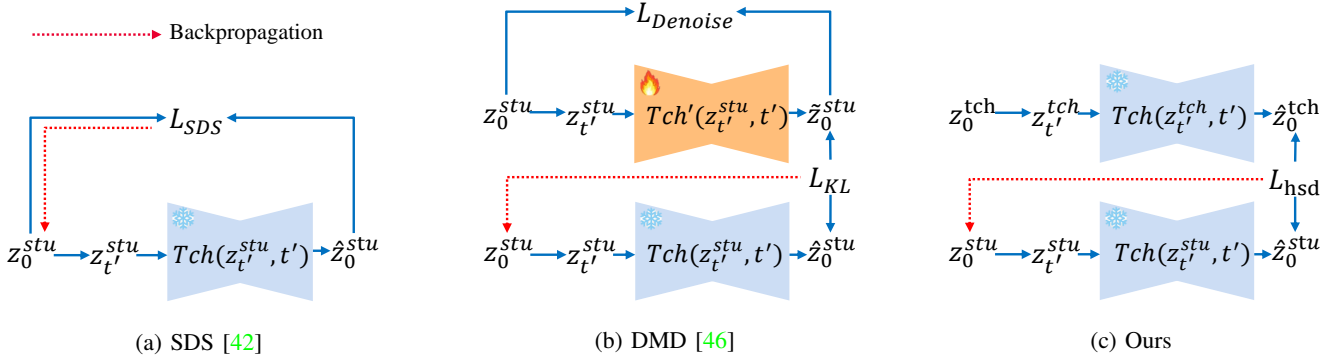


Fig. 4: Comparison of various score distillation techniques. Compared to SDS [22], [42] and DMD [46], our HF-enhanced score distillation fully utilizes the potential of teacher model, providing meaningful gradient guidance to student models without the need to retrain a new diffusion model.

B. TAD-SR

The overview framework of our proposed TAD-SR is illustrated in Fig. 3, consisting of a teacher model F_ϕ parameterized by ϕ , a student network f_θ initialized from the teacher model with weights θ , and a trainable time-aware discriminator D_ψ parameterized by ψ . During training, the student model generates samples from noisy data and computes the mean squared loss against the samples generated iteratively by the teacher model. Subsequently, we introduce slight noise to the samples produced by both the student and teacher models, predict the score function via the teacher model, and refine the student network by leveraging the discrepancy between the two score functions. Furthermore, to mitigate the performance constraints of the teacher model on the student model, we design a time-aware discriminator built upon the encoder of the pre-trained teacher model, enhancing the perceptual quality of the generated samples through adversarial training processes.

Vanilla distillation. We utilize the multi-step output results of the teacher model as the learning objective for the student model. It guides the student model to establish a mapping between low-resolution and high-resolution images through single-step inference. The distillation loss is formulated as follows:

$$\mathcal{L}_{distill} = \|F_\phi(z_T, T, y) - f_\theta(z_T, T, y)\|_2^2 \quad (6)$$

where z_T is obtained through the forward process Eq. (1). Specifically, when time step $t = T$, noisy latent $z_T \sim \mathcal{N}(x_t; y, \kappa^2 \eta_t \mathbf{I})$.

High-frequency enhanced score distillation. As analyzed in Section IV-A, employing SDS [42] to accelerate diffusion-based SR models is not an optimal solution. Its inherent bias may introduce meaningless gradient directions to the student model, leading to output blurring, oversaturation, and other issues [44], [45]. To eliminate this bias, DMD [46] trains a new diffusion model to learn the score function of samples generated by the student model and updates the generator based on the difference between the score functions predicted by the new model and the teacher model. However, this approach involves a complex training process that requires alternating training between the student model and the new diffusion model.

By contrast, based on the observations presented in Fig. 2, we develop an effective and efficient score distillation method. Specifically, we analyze the score differences between the outputs of the teacher model and the student model under various noise disturbances. Experiments indicate that these differences are primarily significant under mild noise disturbances (i.e., small time steps). Given that diffusion models typically predict high-frequency information in images at small time steps, this suggests that images generated by student models are predominantly deficient in high-frequency details compared to those produced by teacher models. Consequently, we propose a high-frequency enhanced score distillation method. This approach optimizes the student model by computing the score differences between the outputs of the teacher model and the student model under slight noise disturbances, thereby enhancing the student model’s ability to accurately capture and reproduce high-frequency details. Specifically, we apply slight Gaussian noise to perturb the outputs of both the student and teacher models and model their data distributions. According to score distillation, the following formula is derived:

$$\mathcal{L}_{hsd} = \mathbb{E}_{z_{t'}^{tch}, z_{t'}^{stu}, y} [\omega (\epsilon_\phi(z_{t'}^{stu}, t, y) - \epsilon_\phi(z_{t'}^{tch}, t, y))], \quad (7)$$

where $\omega = 1/CS$ is a weighting function, C is the number of channels and S is the number of spatial pixels. $z_{t'}^{tch}$ and $z_{t'}^{stu}$ are the noise data obtained by adding noise to the outputs of the teacher model z_0^{tch} and the output of student model z_0^{stu} , respectively, through Eq. 1. Since we primarily supplement the high-frequency details of the generated images of the student model, time step t' in Eq. 1 are uniformly sampled in [1, 3]. Note that during the loss backpropagation in Eq. 7, similar to SDS [42], we omit the U-Net Jacobian matrix term. According to Eq. 1, we can simplify Eq. 7 as the following formula:

$$\mathcal{L}_{hsd} = \omega_2 (z_0^{stu} - z_0^{tch} + F_\phi(z_{t'}^{tch}, t, y) - F_\phi(z_{t'}^{stu}, t, y)). \quad (8)$$

where $\omega_2 = \frac{\omega(1-\eta_{t'})}{\sqrt{\eta_{t'}\kappa}}$. The details of the derivation can be found in the appendix.

From the above equation, it can be seen that when the output of the student model is the same as that of the teacher model, the loss is zero, and there is no additional bias. Compared to SDS [22], [42], our proposed score distillation provides more meaningful gradient guidance for student models.

Time-aware adversarial loss. ADD [22] has demonstrated that combining diffusion models with generative adversarial networks can significantly improve the perceptual quality of generated images. However, this approach relies on pre-training the DINOv2 discriminator in pixel space, which is both costly and complex. To reduce training costs and enhance model performance, LADD [39] employed a pre-trained diffusion model for generative adversarial training in latent space. Although LADD reduces the training costs associated with adversarial diffusion distillation, it overlooks the significant correlation between the features extracted by the diffusion model and the time steps. By employing only a single discriminator, which lacks any temporal information, to differentiate between the distribution differences of real and synthetic data across various noise disturbances, LADD introduces a challenge to the optimization of the discriminator. To address this issue, we propose a time-aware discriminator, which is capable of distinguishing between the data distributions of real and generated images that have undergone various perturbations in latent space. Specifically, we first utilize the encoder part of the teacher model to extract multi-scale features F_k from both the student model’s output images and real images.

$$F_k = Enc_\phi(z_t, t, y), \quad (9)$$

where Enc_ϕ denotes the encoder part of the teacher model, z_t represents the noisy latent code after adding noise to the student model output or the real latent code. We use F_k^{stu} and F_k^{gt} to denote the features extracted from real latent code and the features extracted from the output of the student model, respectively. We then encode the time step t and map it to a set of time embeddings corresponding to the multi-scale feature dimensions using several linear layers. These time embeddings are used to modulate the features:

$$\hat{F}_k = Norm(F_k) * (1 + \gamma_k) + \beta_k, \quad (10)$$

where γ_k and β_k is a set of learnable modulation parameters produced by projecting time step t into embedding space. After modulation, features of different scales are sent to various discrimination heads $D_{\psi,k}$ for evaluation. The final output is obtained by averaging the results from each discrimination head. The corresponding adversarial loss can be formulated as follows:

$$\mathcal{L}_{adv}^{f_\theta} = -\mathbb{E}_{z_0^{stu}} \left[\sum_k D_{\psi,k}(\hat{F}_k^{stu}) \right], \quad (11)$$

$$\begin{aligned} \mathcal{L}_{adv}^{D_\psi} &= \mathbb{E}_{z_0^{stu}} \left[\sum_k \max\left(0, 1 + D_{\psi,k}(\hat{F}_k^{stu})\right) \right] \\ &+ \mathbb{E}_{z_0} \left[\sum_k \max\left(0, 1 - D_{\psi,k}(\hat{F}_k)\right) \right] \end{aligned} \quad (12)$$

The total objective. The student network is trained with the above three losses as follows:

$$\mathcal{L}_{f_\theta} = \mathcal{L}_{distill} + \lambda_1 \mathcal{L}_{hsd} + \lambda_2 \mathcal{L}_{adv}^{f_\theta}, \quad (13)$$

where λ_1 and λ_2 are the hyperparameters to control the relative importance of these objectives.

V. EXPERIMENTS

A. Experimental Setup

Training Details. For a fair comparison, we follow the same experimental setup and backbone design as that in [9], [18]. Specifically, we use the weights of the teacher model (ResShift) to initialize the student model, and then train the model for 30K iterations based on our proposed loss functions. For the real-world image super-resolution task, we set the weighting factor $\lambda_1 = 1$ and $\lambda_2 = 0.02$. For the blind face restoration task, we set $\lambda_1 = 0.1$ and $\lambda_2 = 0.2$.

Compared methods. For real-world SR task, we evaluate the effectiveness and efficiency of TAD-SR in comparison to several representative SR models, including BSRGAN [12], SwinIR [14], RealESRGAN [13], DASR [15], LDM [16], ResShift [9] and SinSR [18]. For blind face restoration task, we compare TAD-SR with seven recent BFR methods, including DFDNet [49], PSFRGAN [50], GFPGAN [51], RestoreFormer [52], VQFR [53], CodeFormer [54], and DiffFace [55].

Metrics. For real-world super-resolution tasks, we utilize PSNR, SSIM [56], and LPIPS [57], CLIPQA [58] and MUSIQ [59] to measure the performance of proposed method. For face blind restoration task, besides the above metrics, we also evaluate methods with identity score (IDS), landmark distance (LMD) and FID. On the real-world datasets, it is worth noting non-reference metrics such as CLIPQA and MUSIQ are more convincing, because they are specifically designed to assess the realism of images in the absence of ground truth.

Datasets. For the real-world image super-resolution task, we train the models on the training set of ImageNet [60] following the same pipeline with ResShift [9] where the degradation model is adopted from RealESRGAN [13]. Then, we evaluate our model on one synthetic dataset ImageNet-Test [9], [60] and two real-world datasets RealSR [61] and RealSet65 [9]. For the blind face restoration task, We train the models on FFHQ dataset [62], and the LQ images are synthesized following a typical degradation model used in [51]. One synthetic dataset CelebA-Test [9], [63] and three real-world datasets LFW [64], WebPhoto and WIDER [65] are adopted to evaluate the performance of face restoration model.

TABLE I: Quantitative results of different methods on the dataset of *ImageNet-Test*. The best and second best results are highlighted in **bold** and underline. * indicates that the result was obtained by replicating the method in the paper. Running time is tested on NVIDIA Telsa A100 GPU on the $\times 4$ (64 \rightarrow 256) SR tasks. The non-trainable parameters, such as the parameters of VQGAN in LDM, are marked with gray color for clarity.

Methods	Metrics				
	LPIPS \downarrow	CLIPQA \uparrow	MUSIQ \uparrow	Runtime (s)	#Params (M)
ESRGAN [47]	0.485	0.451	43.615	0.038	16.70
RealSR-JPEG [48]	0.326	0.537	46.981	0.038	16.70
BSRGAN [12]	0.259	0.581	54.697	0.038	16.70
SwinIR [14]	0.238	0.564	53.790	0.107	28.01
RealESRGAN [13]	0.254	0.523	52.538	0.038	16.70
DASR [15]	0.250	0.536	48.337	0.022	8.06
LDM-15 [16]	0.269	0.512	46.419	0.408	113.60 + 55.32
StableSR-15 [17]	0.262	0.659	59.443	1.070	52.49 + 1422.49
ResShift-15 [9]	0.231	0.592	53.660	0.682	118.59 + 55.32
SinSR-1 [18]	0.221	0.611	53.357	0.058	118.59 + 55.32
SinSR*-1	0.231	0.599	52.462	0.058	118.59 + 55.32
<i>TAD-SR-1</i>	<u>0.227</u>	<u>0.652</u>	<u>57.533</u>	0.058	118.59 + 57.32

TABLE II: Quantitative results of different methods on two real-world datasets. The best and second best results are highlighted in **bold** and underline.

Methods	Datasets			
	<i>RealSR</i>		<i>RealSet65</i>	
	CLIPQA \uparrow	MUSIQ \uparrow	CLIPQA \uparrow	MUSIQ \uparrow
ESRGAN [47]	0.236	29.048	0.374	42.369
RealSR-JPEG [48]	0.362	36.076	0.528	50.539
BSRGAN [12]	0.543	<u>63.586</u>	0.616	<u>65.582</u>
SwinIR [14]	0.465	59.636	0.578	63.822
RealESRGAN [13]	0.490	59.678	0.600	63.220
DASR [15]	0.363	45.825	0.497	55.708
LDM-15 [16]	0.384	49.317	0.427	47.488
StableSR-15 [17]	0.493	59.634	0.531	56.301
ResShift-15 [9]	0.596	59.873	0.654	61.330
SinSR-1 [18]	0.689	61.582	<u>0.715</u>	62.169
SinSR*-1	<u>0.691</u>	60.865	0.712	62.575
<i>TAD-SR-1</i>	0.741	65.701	0.734	67.500

B. Experimental Results

Evaluation on synthetic datasets. For the real-world SR task, we conducted a comprehensive comparison between TAD-SR and other state-of-the-art methods on the ImageNet-Test dataset, as summarized in Table I and Fig. 5. The following conclusions can be drawn: i) TAD-SR significantly outperforms other methods in terms of non-reference metrics, specifically CLIPQA and MUSIQ, and achieves second-best results in the full-reference metric LPIPS. It demonstrates the effectiveness of the proposed method. ii) The substantial improvement in non-reference metrics indicates that TAD-SR has the ability to generate images with high perceptual quality and realism. iii) Visual results show that TAD-SR produces images with higher clarity and better visual perception. In summary, the proposed TAD-SR effectively distills the teacher model of ResShift into a single step, generating more realistic image results while maintaining comparable fidelity to the teacher model. For blind face restoration, We used CelebA-Test as the testing dataset, and results are summarized in Table III and Fig. 6. From the perspective of evaluation metrics, the proposed method achieves state-of-the-art results in terms of FID and comparable results in terms of IDS, LDM, CLIPQA, and MUSIQ, which demonstrates the effectiveness of TAD-SR on blind face restoration. From the visualization

results, the generated faces by the proposed method appear more natural and exhibit richer details. For example, in the images of Fig. 6, the results of TAD-SR show more natural and realistic hair, while the facial clarity is higher, with complete and rich details.

Evaluation on real-world datasets. For the SR task, in addition to evaluating our method on synthetic datasets, we also evaluated the method in real-world scenarios, and results are reported in Table II. As shown in the table, in terms of the CLIPQA and MUSIQ metrics, the proposed method significantly outperforms other methods with just a single-step inference. Specifically, compared to the ResShift 15-step model serving as our teacher model, these non-reference metrics show a significant improvement after applying TAD-SR. Additionally, visual comparisons are displayed in Fig. 8. To ensure a comprehensive evaluation, we try to include diverse scenarios, such as buildings, animals, and letters. It can be observed that the images generated by TAD-SR appear more naturalistic, as evidenced by the distinct brick textures, as well as the fine and natural-looking polar bear fur. For blind face restoration, we evaluated recent methods on three datasets: LFW, Webphoto, and WIDER. The results are presented in Table IV, and significant conclusions can be drawn as follows. On all three datasets, the proposed method achieves the best

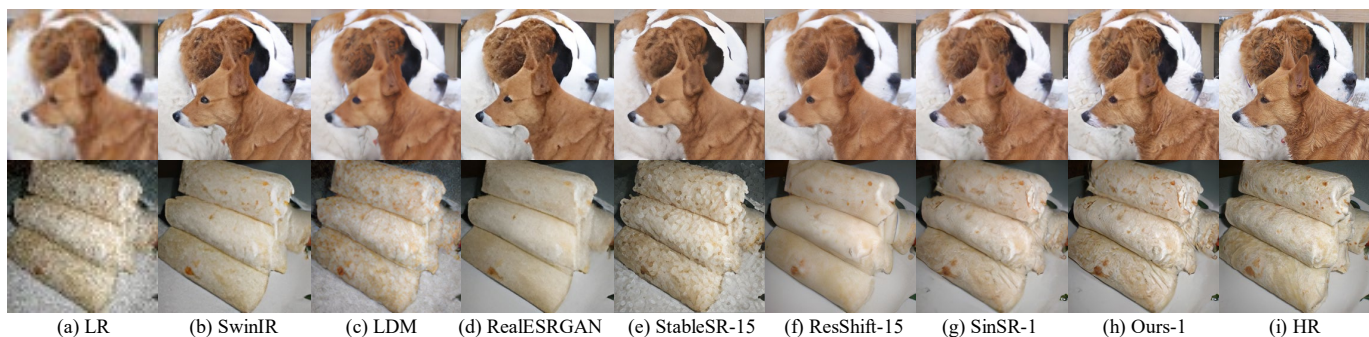


Fig. 5: Qualitative comparisons of different methods on two synthetic examples of the *ImageNet-Test* dataset. Please zoom in for a better view.

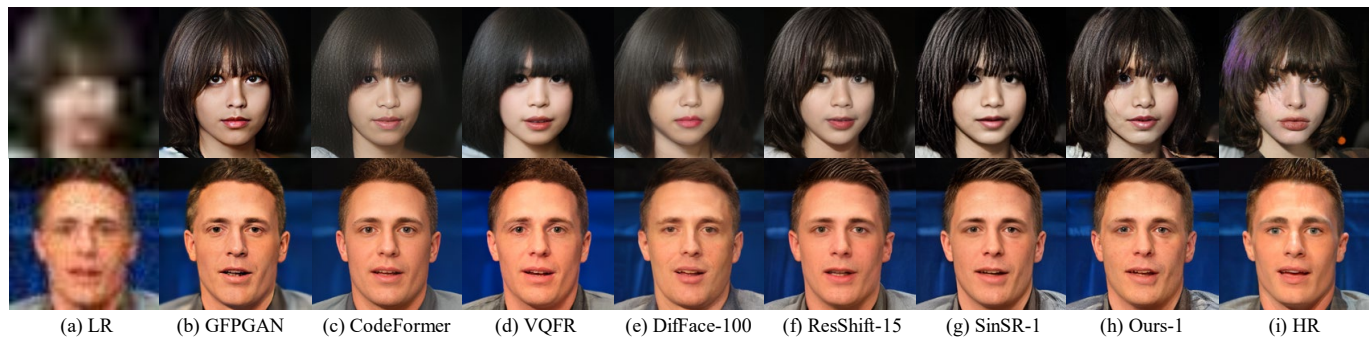


Fig. 6: Qualitative comparisons of different methods on two synthetic examples of the *CelebA-Test* dataset. Please zoom in for a better view.

TABLE III: Quantitative results of different methods on the dataset of *CelebA-Test*. The best and second best results are highlighted in **bold** and underline.

Methods	Metrics						
	LPIPS↓	IDS↓	LMD↓	FID-F↓	FID-G↓	CLIQQA↑	MUSIQ↑
DFDNet [49]	0.739	86.323	20.784	93.621	76.118	0.619	51.173
PSFRGAN [50]	0.475	74.025	10.168	63.676	60.748	0.630	69.910
GFPGAN [51]	0.416	66.820	8.886	66.308	27.698	0.671	<u>75.388</u>
RestoreFormer [52]	0.488	70.518	11.137	50.165	51.997	0.736	71.039
VQFR [53]	0.411	65.538	8.910	58.423	25.234	0.685	73.155
CodeFormer [54]	0.324	59.136	5.035	62.794	26.160	0.698	75.900
DiffFace-100 [55]	0.338	63.033	5.301	52.531	23.212	0.527	66.042
ResShift-4 [9]	0.309	<u>59.623</u>	5.056	<u>50.164</u>	<u>17.564</u>	0.613	73.214
SinSR*-1 [18]	<u>0.319</u>	60.305	4.935	55.292	21.681	0.634	74.140
<i>TAD-SR-1</i>	0.341	59.897	<u>5.050</u>	41.968	16.779	0.735	75.027

CLIQQA, which outperforms the other methods by a large margin. On the WIDER dataset, the proposed method achieves the second-best MUSIQ. All these results inform that in terms of blind face restoration, TAD-SR can generate images with really high perceptual quality. We provide visual comparisons in Fig. 11. It can be observed that the results obtained by TAD-SR show more realistic hair details, clearer facial contours, and better skin textures.

C. Ablation Study

The aforementioned experiments have confirmed the effectiveness of our method in image super-resolution tasks. This section is dedicated to presenting ablation studies that aim to further validate the importance of the crucial modules introduced within our framework.

High-frequency enhanced score distillation. We first investigate the importance of high-frequency enhanced score distillation. Recall that in Section IV-B, we analyzed how high-frequency enhanced score distillation can provide a meaningful guidance for optimizing student model compared to score distillation sampling (SDS). Here, we further validate its effectiveness on real-world benchmarks. As shown in Table V, compared with SDS, our proposed high-frequency enhanced score distillation can significantly improved the CLIQQA and MUSIQ scores on both the RealSR and RealSet65 datasets. This indicates that our proposed high-frequency enhanced score distillation can indeed improve the quality of image generation and is superior to SDS.

Time-aware discriminator. It has been proven that introducing generative adversarial training in latent space is easier to optimize and more cost-effective compared to pixel space

TABLE IV: Quantitative results of different methods on three real-world human face datasets. The best and second best results are highlighted in **bold** and underline.

Methods	Datasets					
	<i>LFW</i>		<i>WebPhoto</i>		<i>WIDER</i>	
	CLIPQA \uparrow	MUSIQ \uparrow	CLIPQA \uparrow	MUSIQ \uparrow	CLIPQA \uparrow	MUSIQ \uparrow
DFDNet [49]	0.716	73.109	0.654	59.024	0.625	63.210
PSFRGAN [50]	0.647	73.602	0.637	71.674	0.648	71.507
GFPGAN [51]	0.687	<u>74.836</u>	0.651	<u>73.369</u>	0.663	74.694
RestoreFormer [52]	<u>0.741</u>	73.704	<u>0.709</u>	69.837	<u>0.730</u>	67.840
VQFR [53]	0.710	74.386	0.677	70.904	0.707	71.411
CodeFormer [54]	0.689	75.480	0.692	74.004	0.699	73.404
DiffFace-100 [55]	0.593	70.362	0.555	65.379	0.561	64.970
ResShift-4 [9]	0.626	70.643	0.621	71.007	0.629	71.084
SinSR*-1 [18]	0.640	72.457	0.641	73.357	0.654	73.556
<i>TAD-SR-1</i>	0.768	74.085	0.718	71.952	0.770	<u>73.739</u>

TABLE V: Ablation studies of the proposed methods on *RealSR* and *RealSet65* benchmarks. The best results are highlighted in **bold**.

Methods	Settings	<i>RealSR/RealSet65</i>	
		CLIPQA \uparrow	MUSIQ \uparrow
(a)	SDS + GAN	0.489/0.528	57.290/57.567
(b)	SDS + t-GAN	0.538/0.554	60.223/59.627
(c)	HSD + GAN	0.711/0.729	63.550/66.904
Ours	HSD + t-GAN	0.741/0.734	65.701/67.500

[39]. Now, we demonstrate the importance of introducing time injection into the discriminator. Intuitively, when the discriminator does not have time injection, it needs to distinguish the distribution between real data and generated data under different noise disturbances, which is undoubtedly extremely challenging. Adding time injection to the discriminator is equivalent to providing additional information related to the level of noise disturbance, which should improve the performance of the discriminator and provide more effective supervision for the generator. We further validated the above analysis through experiments. As shown in Table V, performance improves with the replacement of the standard discriminator by our proposed time-aware discriminator, regardless of the score distillation technique used.

VI. CONCLUSION

In this paper, we propose a time-aware distillation method that accelerates diffusion-based super-resolution models to a single inference step. We introduce a high-frequency enhanced score distillation technique that optimizes the generator by calculating the score difference between the outputs of the teacher and student models following noise perturbation, thereby enhancing the high-frequency details in the student model’s output. To elevate the student model’s performance ceiling, we incorporate generative adversarial learning into the diffusion model framework. Specifically, we design a time-aware discriminator that distinguishes between generated and real data in latent space, providing more efficient and effective supervision for the student model. Extensive experiments demonstrate that our method can achieve performance on par with or surpassing that of the teacher model in a single inference step.

REFERENCES

- [1] J. Ho, A. Jain, and P. Abbeel, “Denoising diffusion probabilistic models,” *Advances in neural information processing systems*, vol. 33, pp. 6840–6851, 2020.
- [2] J. Song, C. Meng, and S. Ermon, “Denoising diffusion implicit models,” *arXiv preprint arXiv:2010.02502*, 2020.
- [3] I. Goodfellow, J. Pouget-Abadie, M. Mirza, B. Xu, D. Warde-Farley, S. Ozair, A. Courville, and Y. Bengio, “Generative adversarial networks,” *Communications of the ACM*, vol. 63, no. 11, pp. 139–144, 2020.
- [4] C. Meng, Y. He, Y. Song, J. Song, J. Wu, J.-Y. Zhu, and S. Ermon, “Sdedit: Guided image synthesis and editing with stochastic differential equations,” *arXiv preprint arXiv:2108.01073*, 2021.
- [5] A. Hertz, R. Mokady, J. Tenenbaum, K. Aberman, Y. Pritch, and D. Cohen-Or, “Prompt-to-prompt image editing with cross attention control,” *arXiv preprint arXiv:2208.01626*, 2022.
- [6] H. Chung, B. Sim, and J. C. Ye, “Come-closer-diffuse-faster: Accelerating conditional diffusion models for inverse problems through stochastic contraction,” in *Proceedings of the IEEE/CVF Conference on Computer Vision and Pattern Recognition*, 2022, pp. 12 413–12 422.
- [7] A. Lugmayr, M. Danelljan, A. Romero, F. Yu, R. Timofte, and L. Van Gool, “Repaint: Inpainting using denoising diffusion probabilistic models,” in *Proceedings of the IEEE/CVF conference on computer vision and pattern recognition*, 2022, pp. 11 461–11 471.
- [8] C. Saharia, J. Ho, W. Chan, T. Salimans, D. J. Fleet, and M. Norouzi, “Image super-resolution via iterative refinement,” *IEEE transactions on pattern analysis and machine intelligence*, vol. 45, no. 4, pp. 4713–4726, 2022.
- [9] Z. Yue, J. Wang, and C. C. Loy, “Resshift: Efficient diffusion model for image super-resolution by residual shifting,” *Advances in Neural Information Processing Systems*, vol. 36, 2024.
- [10] J. Choi, S. Kim, Y. Jeong, Y. Gwon, and S. Yoon, “Ilvr: Conditioning method for denoising diffusion probabilistic models,” *arXiv preprint arXiv:2108.02938*, 2021.
- [11] B. Fei, Z. Lyu, L. Pan, J. Zhang, W. Yang, T. Luo, B. Zhang, and B. Dai, “Generative diffusion prior for unified image restoration and enhancement,” in *Proceedings of the IEEE/CVF Conference on Computer Vision and Pattern Recognition*, 2023, pp. 9935–9946.
- [12] K. Zhang, J. Liang, L. Van Gool, and R. Timofte, “Designing a practical degradation model for deep blind image super-resolution,” in *Proceedings of the IEEE/CVF International Conference on Computer Vision*, 2021, pp. 4791–4800.
- [13] X. Wang, L. Xie, C. Dong, and Y. Shan, “Real-esrgan: Training real-world blind super-resolution with pure synthetic data,” in *Proceedings of the IEEE/CVF international conference on computer vision*, 2021, pp. 1905–1914.
- [14] J. Liang, J. Cao, G. Sun, K. Zhang, L. Van Gool, and R. Timofte, “Swinir: Image restoration using swin transformer,” in *Proceedings of the IEEE/CVF international conference on computer vision*, 2021, pp. 1833–1844.
- [15] J. Liang, H. Zeng, and L. Zhang, “Efficient and degradation-adaptive network for real-world image super-resolution,” in *European Conference on Computer Vision*. Springer, 2022, pp. 574–591.
- [16] R. Rombach, A. Blattmann, D. Lorenz, P. Esser, and B. Ommer, “High-resolution image synthesis with latent diffusion models,” in *Proceedings of the IEEE/CVF conference on computer vision and pattern recognition*, 2022, pp. 10 684–10 695.

- [17] J. Wang, Z. Yue, S. Zhou, K. C. Chan, and C. C. Loy, "Exploiting diffusion prior for real-world image super-resolution," *arXiv preprint arXiv:2305.07015*, 2023.
- [18] Y. Wang, W. Yang, X. Chen, Y. Wang, L. Guo, L.-P. Chau, Z. Liu, Y. Qiao, A. C. Kot, and B. Wen, "Sinsr: Diffusion-based image super-resolution in a single step," *arXiv preprint arXiv:2311.14760*, 2023.
- [19] C. Lu, Y. Zhou, F. Bao, J. Chen, C. Li, and J. Zhu, "Dpm-solver: A fast ode solver for diffusion probabilistic model sampling in around 10 steps," *Advances in Neural Information Processing Systems*, vol. 35, pp. 5775–5787, 2022.
- [20] K. Zheng, C. Lu, J. Chen, and J. Zhu, "Dpm-solver-v3: Improved diffusion ode solver with empirical model statistics," *Advances in Neural Information Processing Systems*, vol. 36, 2024.
- [21] T. Salimans and J. Ho, "Progressive distillation for fast sampling of diffusion models," *arXiv preprint arXiv:2202.00512*, 2022.
- [22] A. Sauer, D. Lorenz, A. Blattmann, and R. Rombach, "Adversarial diffusion distillation," *arXiv preprint arXiv:2311.17042*, 2023.
- [23] R. Xie, Y. Tai, K. Zhang, Z. Zhang, J. Zhou, and J. Yang, "Addsr: Accelerating diffusion-based blind super-resolution with adversarial diffusion distillation," *arXiv preprint arXiv:2404.01717*, 2024.
- [24] W. Dong, L. Zhang, G. Shi, and X. Li, "Nonlocally centralized sparse representation for image restoration," *IEEE transactions on Image Processing*, vol. 22, no. 4, pp. 1620–1630, 2012.
- [25] S. Gu, Q. Xie, D. Meng, W. Zuo, X. Feng, and L. Zhang, "Weighted nuclear norm minimization and its applications to low level vision," *International journal of computer vision*, vol. 121, pp. 183–208, 2017.
- [26] S. Gu, W. Zuo, Q. Xie, D. Meng, X. Feng, and L. Zhang, "Convolutional sparse coding for image super-resolution," in *Proceedings of the IEEE International Conference on Computer Vision*, 2015, pp. 1823–1831.
- [27] W.-S. Lai, J.-B. Huang, N. Ahuja, and M.-H. Yang, "Deep laplacian pyramid networks for fast and accurate super-resolution," in *Proceedings of the IEEE conference on computer vision and pattern recognition*, 2017, pp. 624–632.
- [28] J. Menick and N. Kalchbrenner, "Generating high fidelity images with subscale pixel networks and multidimensional upscaling," *arXiv preprint arXiv:1812.01608*, 2018.
- [29] A. Lugmayr, M. Danelljan, L. Van Gool, and R. Timofte, "SrfLOW: Learning the super-resolution space with normalizing flow," in *Computer Vision—ECCV 2020: 16th European Conference, Glasgow, UK, August 23–28, 2020, Proceedings, Part V 16*. Springer, 2020, pp. 715–732.
- [30] M. S. Sajjadi, B. Scholkopf, and M. Hirsch, "Enhancenet: Single image super-resolution through automated texture synthesis," in *Proceedings of the IEEE international conference on computer vision*, 2017, pp. 4491–4500.
- [31] X. Pan, X. Zhan, B. Dai, D. Lin, C. C. Loy, and P. Luo, "Exploiting deep generative prior for versatile image restoration and manipulation," *IEEE Transactions on Pattern Analysis and Machine Intelligence*, vol. 44, no. 11, pp. 7474–7489, 2021.
- [32] K. C. Chan, X. Wang, X. Xu, J. Gu, and C. C. Loy, "Glean: Generative latent bank for large-factor image super-resolution," in *Proceedings of the IEEE/CVF conference on computer vision and pattern recognition*, 2021, pp. 14 245–14 254.
- [33] Y. Zhou, W. Deng, T. Tong, and Q. Gao, "Guided frequency separation network for real-world super-resolution," in *Proceedings of the IEEE/CVF Conference on Computer Vision and Pattern Recognition Workshops*, 2020, pp. 428–429.
- [34] D. Fuoli, L. Van Gool, and R. Timofte, "Fourier space losses for efficient perceptual image super-resolution," in *Proceedings of the IEEE/CVF International Conference on Computer Vision*, 2021, pp. 2360–2369.
- [35] K. Zhang, W. Zuo, and L. Zhang, "Learning a single convolutional super-resolution network for multiple degradations," in *Proceedings of the IEEE conference on computer vision and pattern recognition*, 2018, pp. 3262–3271.
- [36] A. Niu, K. Zhang, T. X. Pham, J. Sun, Y. Zhu, I. S. Kweon, and Y. Zhang, "Cdpmr: Conditional diffusion probabilistic models for single image super-resolution," in *2023 IEEE International Conference on Image Processing (ICIP)*. IEEE, 2023, pp. 615–619.
- [37] S. Gao, X. Liu, B. Zeng, S. Xu, Y. Li, X. Luo, J. Liu, X. Zhen, and B. Zhang, "Implicit diffusion models for continuous super-resolution," in *Proceedings of the IEEE/CVF conference on computer vision and pattern recognition*, 2023, pp. 10 021–10 030.
- [38] T. Yang, P. Ren, X. Xie, and L. Zhang, "Pixel-aware stable diffusion for realistic image super-resolution and personalized stylization," *arXiv preprint arXiv:2308.14469*, 2023.
- [39] A. Sauer, F. Boesel, T. Dockhorn, A. Blattmann, P. Esser, and R. Rombach, "Fast high-resolution image synthesis with latent adversarial diffusion distillation," *arXiv preprint arXiv:2403.12015*, 2024.
- [40] Y. Song, P. Dhariwal, M. Chen, and I. Sutskever, "Consistency models," *arXiv preprint arXiv:2303.01469*, 2023.
- [41] S. Luo, Y. Tan, L. Huang, J. Li, and H. Zhao, "Latent consistency models: Synthesizing high-resolution images with few-step inference," *arXiv preprint arXiv:2310.04378*, 2023.
- [42] B. Poole, A. Jain, J. T. Barron, and B. Mildenhall, "Dreamfusion: Text-to-3d using 2d diffusion," *arXiv preprint arXiv:2209.14988*, 2022.
- [43] C.-H. Lin, J. Gao, L. Tang, T. Takikawa, X. Zeng, X. Huang, K. Kreis, S. Fidler, M.-Y. Liu, and T.-Y. Lin, "Magic3d: High-resolution text-to-3d content creation," in *Proceedings of the IEEE/CVF Conference on Computer Vision and Pattern Recognition*, 2023, pp. 300–309.
- [44] A. Hertz, K. Aberman, and D. Cohen-Or, "Delta denoising score," in *Proceedings of the IEEE/CVF International Conference on Computer Vision*, 2023, pp. 2328–2337.
- [45] Z. Wang, C. Lu, Y. Wang, F. Bao, C. Li, H. Su, and J. Zhu, "Prolificdreamer: High-fidelity and diverse text-to-3d generation with variational score distillation," *Advances in Neural Information Processing Systems*, vol. 36, 2024.
- [46] T. Yin, M. Gharbi, R. Zhang, E. Shechtman, F. Durand, W. T. Freeman, and T. Park, "One-step diffusion with distribution matching distillation," *arXiv preprint arXiv:2311.18828*, 2023.
- [47] X. Wang, K. Yu, S. Wu, J. Gu, Y. Liu, C. Dong, Y. Qiao, and C. Change Loy, "Esrgan: Enhanced super-resolution generative adversarial networks," in *Proceedings of the European conference on computer vision (ECCV) workshops*, 2018, pp. 0–0.
- [48] X. Ji, Y. Cao, Y. Tai, C. Wang, J. Li, and F. Huang, "Real-world super-resolution via kernel estimation and noise injection," in *proceedings of the IEEE/CVF conference on computer vision and pattern recognition workshops*, 2020, pp. 466–467.
- [49] X. Li, C. Chen, S. Zhou, X. Lin, W. Zuo, and L. Zhang, "Blind face restoration via deep multi-scale component dictionaries," in *Proceedings of the European Conference on Computer Vision (ECCV)*, 2020.
- [50] C. Chen, X. Li, L. Yang, X. Lin, L. Zhang, and K.-Y. K. Wong, "Progressive semantic-aware style transformation for blind face restoration," in *Proceedings of the IEEE/CVF Conference on Computer Vision and Pattern Recognition (CVPR)*, 2021.
- [51] X. Wang, Y. Li, H. Zhang, and Y. Shan, "Towards real-world blind face restoration with generative facial prior," in *Proceedings of the IEEE/CVF Conference on Computer Vision and Pattern Recognition (CVPR)*, 2021, pp. 9168–9178.
- [52] Z. Wang, J. Zhang, R. Chen, W. Wang, and P. Luo, "Restoreformer: High-quality blind face restoration from undegraded key-value pairs," in *Proceedings of the IEEE/CVF Conference on Computer Vision and Pattern Recognition (CVPR)*, 2022.
- [53] Y. Gu, X. Wang, L. Xie, C. Dong, G. Li, Y. Shan, and M.-M. Cheng, "Vqfr: Blind face restoration with vector-quantized dictionary and parallel decoder," in *Proceedings of the European Conference on Computer Vision (ECCV)*, 2022, pp. 126–143.
- [54] S. Zhou, K. Chan, C. Li, and C. C. Loy, "Towards robust blind face restoration with codebook lookup transformer," in *Proceedings of Advances in Neural Information Processing Systems (NeurIPS)*, 2022.
- [55] Z. Yue and C. C. Loy, "Difface: Blind face restoration with diffused error contraction," *arXiv preprint arXiv:2212.06512*, 2022.
- [56] Z. Wang, A. C. Bovik, H. R. Sheikh, and E. P. Simoncelli, "Image quality assessment: from error visibility to structural similarity," *IEEE Transactions on Image Processing (TIP)*, vol. 13, no. 4, pp. 600–612, 2004.
- [57] R. Zhang, P. Isola, A. A. Efros, E. Shechtman, and O. Wang, "The unreasonable effectiveness of deep features as a perceptual metric," in *Proceedings of the IEEE/CVF Conference on Computer Vision and Pattern Recognition (CVPR)*, 2018, pp. 586–595.
- [58] J. Wang, K. C. Chan, and C. C. Loy, "Exploring clip for assessing the look and feel of images," in *Proceedings of the AAAI Conference on Artificial Intelligence*, 2023.
- [59] J. Ke, Q. Wang, Y. Wang, P. Milanfar, and F. Yang, "Musiq: Multi-scale image quality transformer," in *Proceedings of the IEEE/CVF International Conference on Computer Vision (ICCV)*, 2021, pp. 5148–5157.
- [60] J. Deng, W. Dong, R. Socher, L.-J. Li, K. Li, and L. Fei-Fei, "Imagenet: A large-scale hierarchical image database," in *2009 IEEE conference on computer vision and pattern recognition*. Ieee, 2009, pp. 248–255.
- [61] J. Cai, H. Zeng, H. Yong, Z. Cao, and L. Zhang, "Toward real-world single image super-resolution: A new benchmark and a new model," in *Proceedings of the IEEE/CVF International Conference on Computer Vision (ICCV)*, 2019, pp. 3086–3095.
- [62] T. Karras, S. Laine, and T. Aila, "A style-based generator architecture for generative adversarial networks," in *Proceedings of the IEEE/CVF*

- Conference on Computer Vision and Pattern Recognition (CVPR)*, 2019, pp. 4401–4410.
- [63] T. Karras, T. Aila, S. Laine, and J. Lehtinen, “Progressive growing of GANs for improved quality, stability, and variation,” in *Proceedings of International Conference on Learning Representations (ICLR)*, 2018.
- [64] G. B. Huang, M. Mattar, T. Berg, and E. Learned-Miller, “Labeled faces in the wild: A database for studying face recognition in unconstrained environments,” in *Workshop on faces in ‘Real-Life’ Images: detection, alignment, and recognition*, 2008.
- [65] S. Yang, P. Luo, C.-C. Loy, and X. Tang, “Wider face: A face detection benchmark,” in *Proceedings of the IEEE/CVF Conference on Computer Vision and Pattern Recognition (CVPR)*, 2016, pp. 5525–5533.
- [66] E. Agustsson and R. Timofte, “Ntire 2017 challenge on single image super-resolution: Dataset and study,” in *Proceedings of the IEEE conference on computer vision and pattern recognition workshops*, 2017, pp. 126–135.
- [67] R. Timofte, E. Agustsson, L. Van Gool, M.-H. Yang, and L. Zhang, “Ntire 2017 challenge on single image super-resolution: Methods and results,” in *Proceedings of the IEEE conference on computer vision and pattern recognition workshops*, 2017, pp. 114–125.
- [68] Y. Li, K. Zhang, J. Liang, J. Cao, C. Liu, R. Gong, Y. Zhang, H. Tang, Y. Liu, D. Demandolx *et al.*, “Lsdir: A large scale dataset for image restoration,” in *Proceedings of the IEEE/CVF Conference on Computer Vision and Pattern Recognition*, 2023, pp. 1775–1787.
- [69] P. Wei, Z. Xie, H. Lu, Z. Zhan, Q. Ye, W. Zuo, and L. Lin, “Component divide-and-conquer for real-world image super-resolution,” in *Computer Vision—ECCV 2020: 16th European Conference, Glasgow, UK, August 23–28, 2020, Proceedings, Part VIII 16*. Springer, 2020, pp. 101–117.
- [70] R. Wu, T. Yang, L. Sun, Z. Zhang, S. Li, and L. Zhang, “Sees: Towards semantics-aware real-world image super-resolution,” in *Proceedings of the IEEE/CVF conference on computer vision and pattern recognition*, 2024, pp. 25 456–25 467.
- [71] J. Liang, H. Zeng, and L. Zhang, “Details or artifacts: A locally discriminative learning approach to realistic image super-resolution,” in *Proceedings of the IEEE/CVF Conference on Computer Vision and Pattern Recognition*, 2022, pp. 5657–5666.
- [72] C. Chen, X. Shi, Y. Qin, X. Li, X. Han, T. Yang, and S. Guo, “Real-world blind super-resolution via feature matching with implicit high-resolution priors,” in *Proceedings of the 30th ACM International Conference on Multimedia*, 2022, pp. 1329–1338.
- [73] S. Yang, T. Wu, S. Shi, S. Lao, Y. Gong, M. Cao, J. Wang, and Y. Yang, “Maniqa: Multi-dimension attention network for no-reference image quality assessment,” in *Proceedings of the IEEE/CVF Conference on Computer Vision and Pattern Recognition*, 2022, pp. 1191–1200.

APPENDIX

A. Implementation Details

1) Mathematical Details

- **Derivation of Eq. (8):** According to the transition distribution of Eq. (1) of our manuscript, the predicted noise ϵ_ϕ can be expressed via the following reparameterization trick:

$$\epsilon_\phi = \frac{z_t - (\hat{z}_0 + \eta_t(z_y - \hat{z}_0))}{\sqrt{\eta_t \kappa}}, \quad (14)$$

where $\hat{z}_0 = F_\phi(z_t, t, y)$. According to the Eq. (14), we can rewrite Eq. (7) as follows:

$$\mathcal{L}_{hsd} = \mathbb{E}_{z_t^{tch}, z_t^{stu}, y} \left[\frac{\omega \left((z_t^{stu} - z_t^{tch}) + (1 - \eta_{t'}) \left(F_\phi(z_t^{tch}, t', y) - F_\phi(z_t^{stu}, t', y) \right) \right)}{\sqrt{\eta_{t'} \kappa}} \right]. \quad (15)$$

Since the noise injected into the output image of the student model and the output image of the teacher model is the same, we have: $z_t^{stu} - z_t^{tch} = (1 - \eta_{t'}) (z_0^{stu} - z_0^{tch})$. Then Eq. (15) can be written as:

$$\begin{aligned} \mathcal{L}_{hsd} &= \mathbb{E}_{z_t^{tch}, z_t^{stu}, y} \left[\frac{\omega (1 - \eta_{t'}) (z_0^{stu} - z_0^{tch} + F_\phi(z_t^{tch}, t', y) - F_\phi(z_t^{stu}, t', y))}{\sqrt{\eta_{t'} \kappa}} \right] \\ &= \mathbb{E}_{z_t^{tch}, z_t^{stu}, y} \left[\omega_2 (z_0^{stu} - z_0^{tch} + F_\phi(z_t^{tch}, t', y) - F_\phi(z_t^{stu}, t', y)) \right], \end{aligned} \quad (16)$$

where $\omega_2 = \frac{\omega(1-\eta_{t'})}{\sqrt{\eta_{t'}}}$

2) TAD-SR Training Procedure

For a comprehensive understanding, we provide a detailed description of our TAD-SR training procedure in Algorithm 1.

B. Experimental Results on SD-based SR method

1) Experimental Setup

In addition to distilling the super-resolution model trained from scratch, we also apply our proposed TAD-SR to distill the SOTA SD-based super-resolution model to further validate its effectiveness.

Training Datasets. We adopt DIV2K [66], Flickr2K [67], first 20K images from LSDIR [68] and first 10K face images from FFHQ [62] for training. The degradation pipeline of Real-ESRGAN [13] is used to synthesize LR-HR training pairs.

Testing Datasets. We evaluate TAD-SR on three real-world datasets: DRealSR [69], RealSR [61], and RealLR200 [70], as well as one synthetic dataset, DIV2K-val [66]. The method for acquiring HR-LR image pairs in the DIV2K dataset follows the procedure detailed in [17], and except RealLR200, all datasets are cropped to 512×512 patches.

Compared Methods. We compare our SeeSR with several state-of-the-art Real-ISR methods, which can be categorized into two groups. The first group consists of GAN-based methods, including BSRGAN [12], Real-ESRGAN [62], LDL [71], FeMaSR [72]. The second group consists of recent diffusion-based methods, including StableSR [17], ResShift [9], PASD [38], SeeSR [70], SinSR [18] and AddSR [23].

Evaluation Metrics. We employ non-reference metrics (e.g., MANIQA [73], MUSIQ [59], CLIPQA [58]) and reference metrics (e.g., LPIPS [35], PSNR, SSIM [56]) to comprehensively evaluate our TAD-SR. Note that in real-world super-resolution tasks, the non-reference metrics is more aligned with human perception and better reflects the subjective quality of images.

2) Evaluation results

We first show the quantitative comparison on the four synthetic and real-world datasets in Tables VI, VII and VIII. The observations from the table are as follows: (1) The GAN-based method shows advantages over diffusion-based methods in full-reference metrics, yet it significantly lags behind diffusion-based methods in non-reference metrics. (2) Our method achieves performance comparable to SeeSR using only single-step sampling. (3) Our method attains optimal or near-optimal performance on non-reference metrics. Additionally, the visualization results demonstrate that our method not only enhances image details with greater clarity (as illustrated in the second row of Fig. 7) but also preserves the similarity to the original image as much as possible (as shown in the fourth row of Fig. 7). Overall, compared to other DM-based methods, our TAD-SR achieves comparable or even superior performance through single-step sampling alone.

C. More visualization results

Algorithm 1: TAD-SR Training Procedure

Input: Pretrained diffusion model F_ϕ , paired dataset $\mathcal{D} = \{x, y\}$, Time steps T
Output: Trained generator f_θ and discriminator D_ψ .

```

1 // Initialize generator from pretrained model
2  $f_\theta \leftarrow \text{copyWeights}(F_\phi)$ ,
3 while train do
4   // Generated images
5   Sample  $\epsilon \sim \mathcal{N}(0, \mathbf{I})$ ,  $(x, y) \sim \mathcal{D}$ 
6    $z_T \leftarrow \text{Forward process}(T, y, x, \epsilon)$  // Eq (1)
7    $z_0^{stu} \leftarrow f_\theta(z_T, y, T)$  // One-step
8    $z_0^{tch} \leftarrow F_\phi(z_T, y, T)$  // Multi-step
9
10  // Update discriminator model
11  Sample time step  $t \sim \mathcal{U}(0, T)$ 
12   $z_t^{stu} \leftarrow \text{Forward process}(t, y, z_0^{stu}, \epsilon)$  // Eq (1)
13   $z_t \leftarrow \text{Forward process}(t, y, x, \epsilon)$  // Eq (1)
14   $\mathcal{L}_{\text{adv}}^{D_\psi} \leftarrow \text{Adversarial loss}(z_t^{stu}, z_t, y, t)$  // Eq (12)
15   $D_\psi \leftarrow \text{update}(D_\psi, \mathcal{L}_{\text{adv}}^{D_\psi})$ 
16
17  // Update generator
18  Sample  $\epsilon' \sim \mathcal{N}(0, \mathbf{I})$ ,  $t' \sim \mathcal{U}(0, T/5)$ 
19   $z_{t'}^{stu} \leftarrow \text{Forward process}(t', y, z_0^{stu}, \epsilon')$  // Eq (1)
20   $z_{t'}^{tch} \leftarrow \text{Forward process}(t', y, z_0^{tch}, \epsilon')$  // Eq (1)
21   $\mathcal{L}_{\text{distill}} \leftarrow \text{Vanilla distillation Loss}(z_0^{stu}, z_0^{tch})$  // Eq (8)
22   $\mathcal{L}_{\text{hsd}} \leftarrow \text{HSD loss}(z_{t'}^{stu}, z_{t'}^{tch}, y, t')$  // Eq (6)
23   $\mathcal{L}_{\text{adv}}^{f_\theta} \leftarrow \text{Adversarial loss}(z_{t'}^{stu}, y, t)$  // Eq (11)
24   $\mathcal{L}_{f_\theta} \leftarrow \mathcal{L}_{\text{distill}} + \lambda_1 \mathcal{L}_{\text{hsd}} + \lambda_2 \mathcal{L}_{\text{adv}}^{f_\theta}$ 
25   $f_\theta \leftarrow \text{update}(f_\theta, \mathcal{L}_{f_\theta})$ 
26 end while

```

TABLE VI: Quantitative comparison with state of the arts on RealSR dataset and RealLR dataset. The best and second best results are highlighted in **bold** and underline. Note that since the RealLR200 dataset lacks real high-resolution images, we only computed non-reference metrics.

Methods	RealSR						RealLR		
	PSNR \uparrow	SSIM \uparrow	LPIPS \downarrow	CLIPQA \uparrow	MUSIQ \uparrow	MANIQA \uparrow	CLIPQA \uparrow	MUSIQ \uparrow	MANIQA \uparrow
BSRGAN [12]	<u>26.49</u>	0.767	0.267	0.512	63.28	0.376	0.570	64.87	0.369
RealESRGAN [13]	25.78	0.762	<u>0.273</u>	0.449	60.36	0.373	0.542	62.93	0.366
LDL [71]	25.09	<u>0.764</u>	0.277	0.430	58.04	0.342	0.509	60.95	0.327
FeMaSR [72]	25.17	0.736	0.294	0.541	59.06	0.361	0.655	64.24	0.410
StableSR-200 [17]	25.63	0.748	0.302	0.528	61.11	0.366	0.592	62.89	0.367
ResShift-15 [9]	26.34	0.735	0.346	0.542	56.06	0.375	0.647	60.25	0.418
PASD-20 [38]	26.67	0.758	0.344	0.519	62.92	0.404	0.620	66.35	0.419
SeeSR-50 (teacher) [70]	25.24	0.720	0.301	<u>0.670</u>	69.82	0.540	0.662	<u>68.63</u>	0.491
SinSR-1 [18]	26.16	0.739	0.308	0.630	60.96	0.399	0.697	63.85	0.445
AddSR-1 [23]	23.12	0.655	0.309	0.552	67.14	0.488	0.585	66.86	0.418
TAD-SR-1 (Ours)	24.50	0.710	0.304	0.676	<u>69.02</u>	<u>0.526</u>	0.674	69.48	<u>0.482</u>

TABLE VII: Quantitative comparison with state of the arts on DRealSR dataset. The best and second best results are highlighted in **bold** and underline.

Methods	DRealSR					
	PSNR \uparrow	SSIM \uparrow	LPIPS \downarrow	CLIPQA \uparrow	MUSIQ \uparrow	MANIQA \uparrow
BSRGAN [12]	28.68	0.802	0.288	0.509	57.17	0.343
RealESRGAN [13]	28.57	<u>0.804</u>	<u>0.285</u>	0.451	54.27	0.343
LDL [71]	27.41	0.807	0.282	0.441	52.38	0.324
FeMaSR [72]	26.83	0.755	0.317	0.564	53.70	0.318
StableSR-200 [17]	29.14	<u>0.804</u>	0.332	0.510	52.28	0.322
ResShift-15 [9]	28.27	0.754	0.401	0.529	50.14	0.328
PASD-20 [38]	<u>29.06</u>	0.791	0.393	0.538	55.33	0.387
SeeSR-50 (teacher) [70]	28.09	0.766	0.319	0.691	65.08	0.513
SinSR-1 [18]	28.32	0.747	0.372	0.642	55.36	0.388
AddSR-1 [23]	26.70	0.738	0.320	0.593	62.13	0.458
TAD-SR-1 (Ours)	27.62	0.767	0.315	<u>0.678</u>	<u>63.43</u>	<u>0.475</u>

TABLE VIII: Quantitative comparison with state of the arts on DIV2k-val dataset. The best and second best results are highlighted in **bold** and underline.

Methods	DIV2K-val					
	PSNR \uparrow	SSIM \uparrow	LPIPS \downarrow	CLIPQA \uparrow	MUSIQ \uparrow	MANIQA \uparrow
BSRGAN [12]	<u>24.58</u>	0.627	0.335	0.524	61.19	0.356
RealESRGAN [13]	24.29	0.637	0.311	0.527	61.06	0.382
LDL [71]	23.83	<u>0.634</u>	0.326	0.518	60.04	0.375
FeMaSR [72]	23.06	0.589	0.346	0.599	60.82	0.346
StableSR-200 [17]	23.29	0.573	<u>0.312</u>	<u>0.676</u>	65.83	0.422
ResShift-15 [9]	24.72	0.623	0.340	0.594	60.89	0.399
PASD-20 [38]	24.51	0.627	0.392	0.551	59.99	0.399
SeeSR-50 (teacher) [70]	23.68	0.604	0.319	0.693	68.68	0.504
SinSR-1 [18]	24.41	0.602	0.324	0.648	62.80	0.424
AddSR-1 [23]	23.26	0.590	0.362	0.573	63.69	0.405
TAD-SR-1 (Ours)	23.54	0.63	0.311	0.664	<u>67.01</u>	<u>0.470</u>

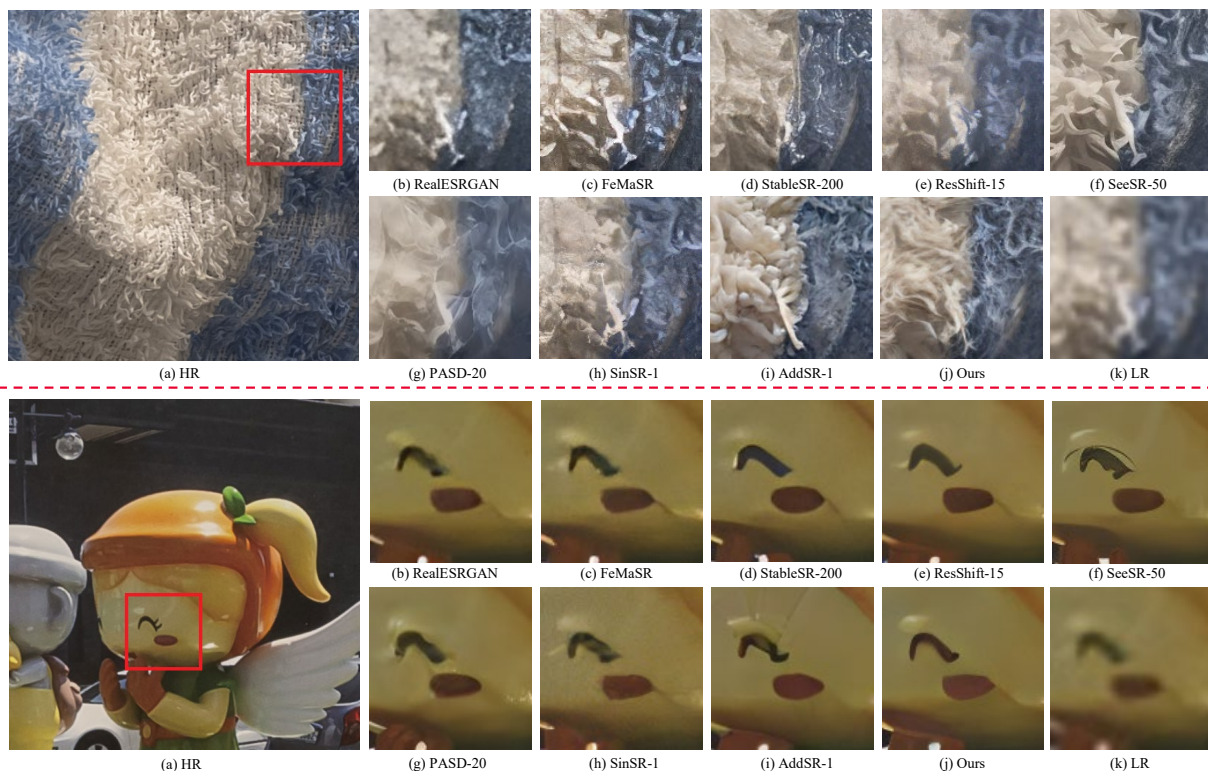


Fig. 7: Visual comparison on real-world LR images. Note that SeeSR is the teacher model.



Fig. 8: Qualitative comparisons of different methods on three real-world examples of the *RealSR* and *RealSet65* dataset. Please zoom in for a better view.

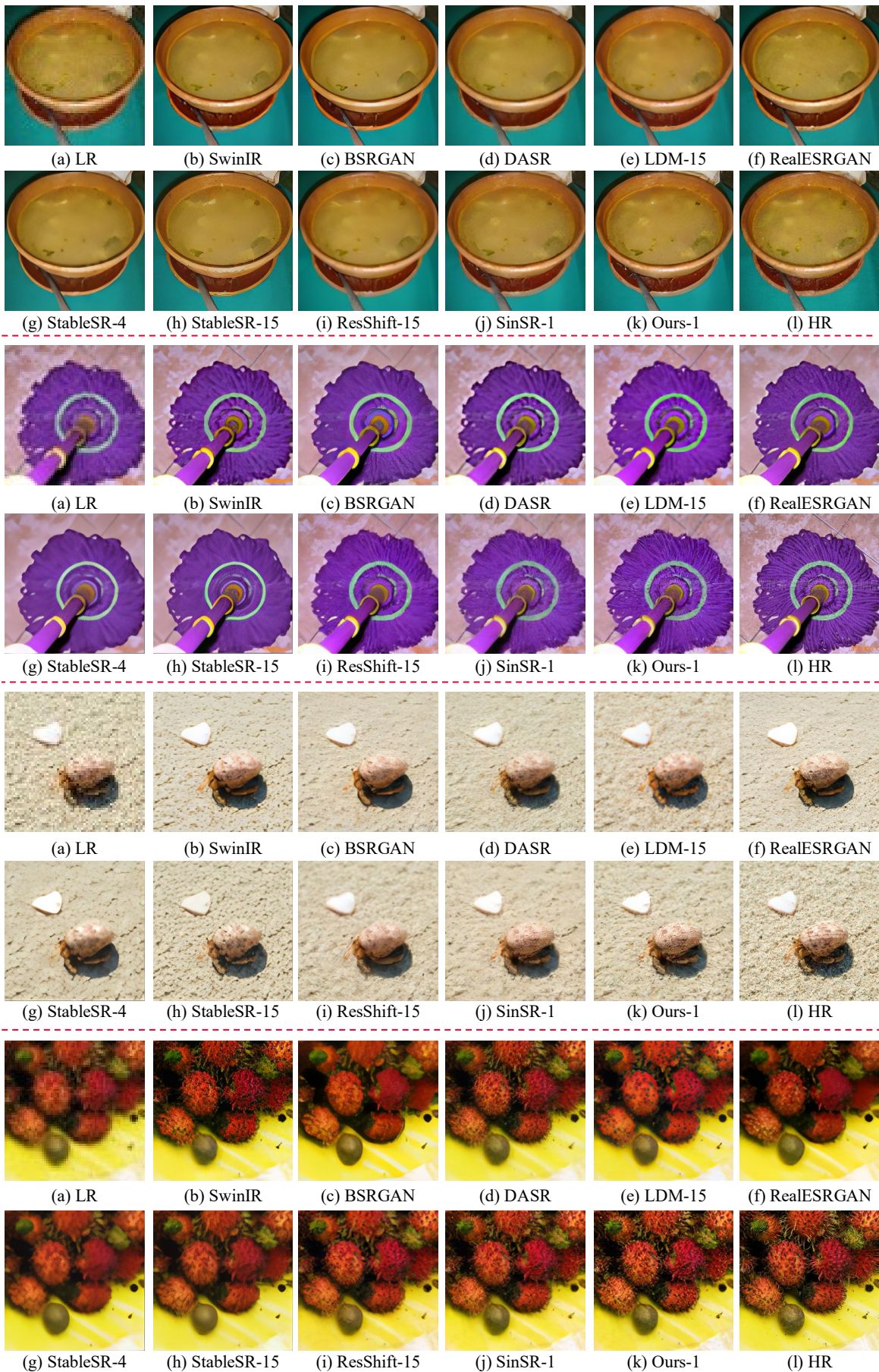


Fig. 9: Qualitative comparisons of different methods on four synthetic examples of the *ImageNet-Test* dataset.

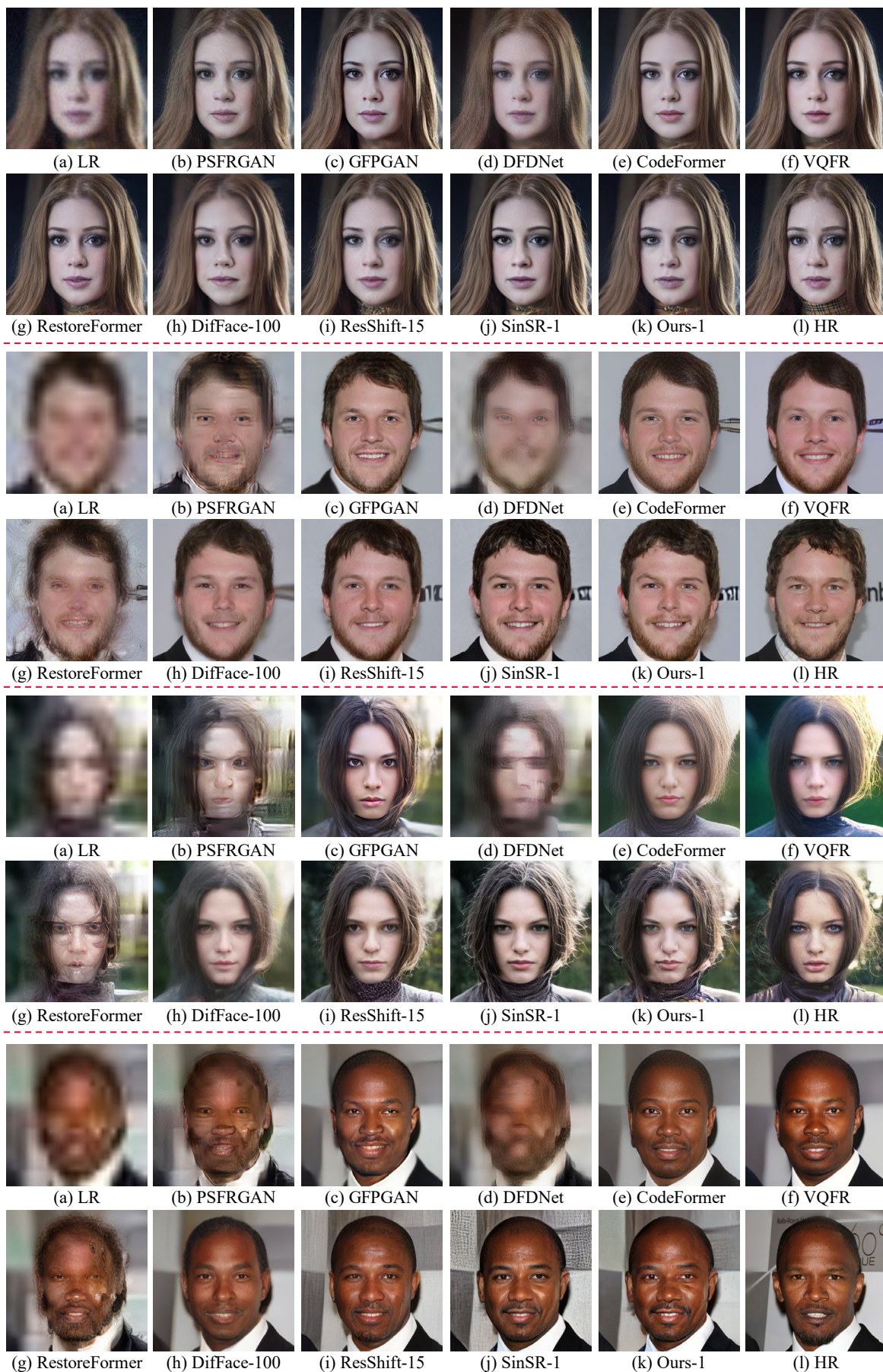


Fig. 10: Qualitative comparisons of different methods on four synthetic examples of the *CelebA-Test* dataset.

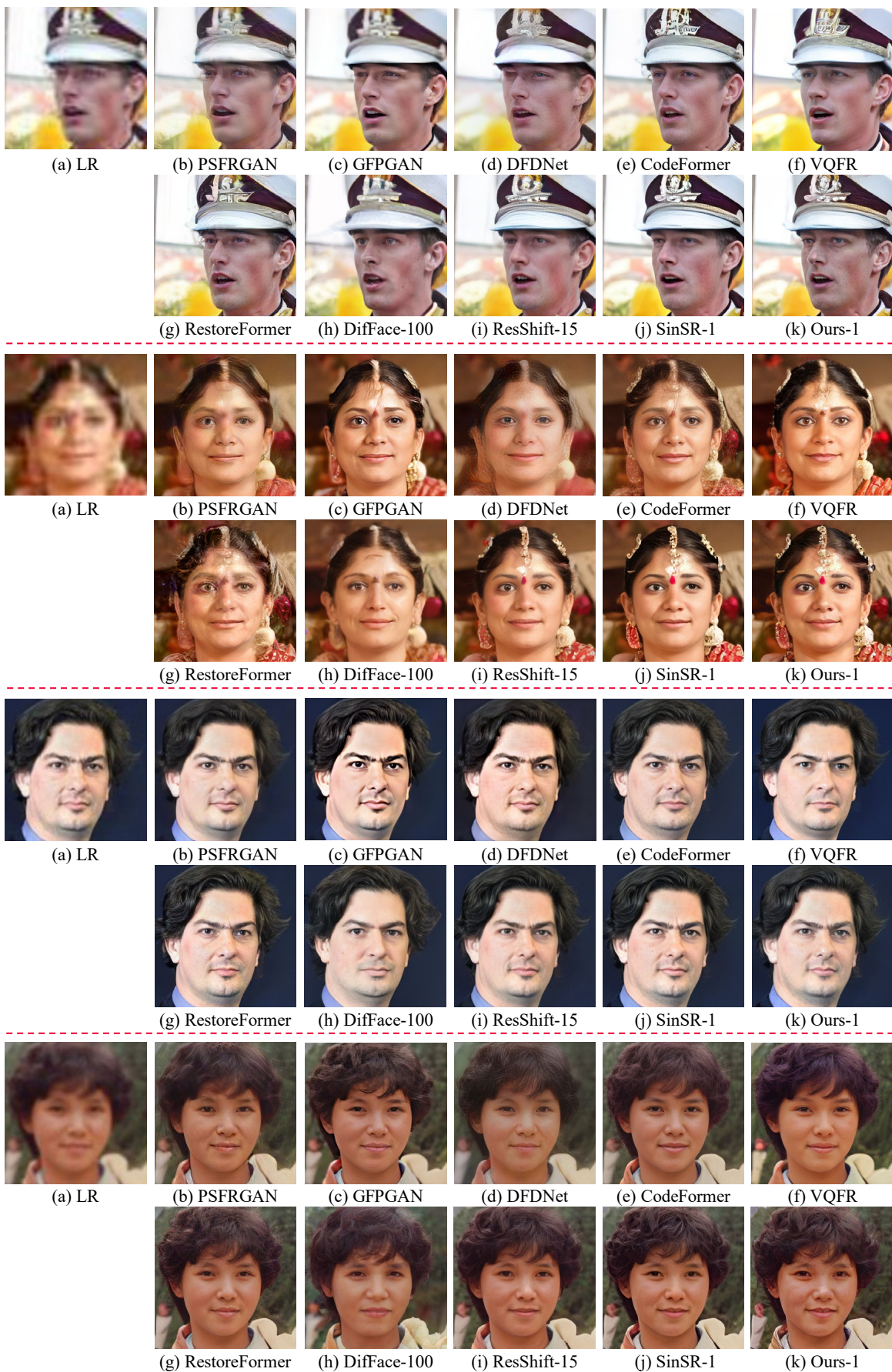


Fig. 11: Qualitative comparisons of different methods on four real-world examples of the *LFW*, *WebPhoto* and *WIDER* dataset.